THERMIONIC EMISSION VS FIELD EMISSION FOR NON-RELATIVISTIC ELECTRON GUNS

Tegan Lisbeth Johnson

Submitted to the faculty of the University Graduate School in partial fulfillment of the requirements for the degree

Master of Science

in the Department of Physics,

Indiana University

March 2019

Accepted by the Graduate Faculty, Indiana University, in partial fulfillment of the requirements for the degree of Master of Science.

Master's Thesis Committee

_____

W. Michael Snow, Ph.D.

_____

Emilio A. Nanni, Ph.D.

_____

David V. Baxter, Ph.D.

Acknowledgements

It is humbling to think of all the opportunities and support I've been given to be able to finally write these words. First and foremost, I owe to my family all that I am and all that I have, or will ever, achieve. This Master's journey itself began with Fermilab and the Department of Energy graciously sending me to my first United States Particle Accelerator School as an intern. I owe so many thanks to Varian Medical Systems, Mark Trail, Steve Vanderet, Rudy Potter, and the rest of the Accelerator Systems group for prioritizing my education and expanding my capabilities. I'm grateful for Bill Barletta, Sami Tantawi, and SLAC for their part in facilitating my research project. I am especially indebted to Emilio Nanni and his unwavering encouragement and patience as my advisor. This juggling act would not have succeeded without him. I would also like to thank W. Michael Snow for advising me from three time zones away, the defense committee for lending me their Valentine's Day morning, Indiana University for sponsoring this Master's program, Susan Winchester for her continuous guidance through this process, and Jason Osheroff for keeping me from running aground during late night USPAS homework sessions. Thank you to the many friends and colleagues involved in the review process. To my roommates, my apologies for monopolizing the kitchen table; I owe you more than a few dinners. And finally, thank you to George Merdinian, for reminding me that I could always hand-calculate the electromagnetic fields like he used to, instead of complaining about my computer.

Tegan Lisbeth Johnson

THERMIONIC VS FIELD EMISSION FOR NON-RELATIVISTIC ELECTRON GUNS

Electron gun design as a whole is a well-studied field, but little research has been done at very low energies, and even less research has been done for asymmetric reentrant cavity designs. Electron guns operating at lower energies require less power and are more efficient, with less ohmic heating. This thesis presents the results of simulated performances of asymmetrical electron gun cathode cavities optimized for shunt impedance and operation at non-relativistic energies. Cavity performance includes current density output, comparing thermionic emission to field emission. An existing Mathematica code for optimizing symmetric cavities at relativistic energies was enhanced for this analysis. For an asymmetric elliptical reentrant cavity designed for 100keV exit energy, with a shunt impedance of 147 MΩ/m: thermionic emission achieved a peak current density of 0.08 A/cm^2, while field emission produced of 1.54 A/cm^2.

1. Introduction

The idea behind a particle accelerator is simple: take a particle, add a force, rinse and repeat. The earliest versions, such as Cockroft-Walton voltage multipliers and Van de Graaff generators, relied on a single electrostatic potential to accelerate particles, but difficulty in maintaining increasingly higher voltages limited the particles' energy [1]. Subsequent accelerators overcame this limitation by accelerating particles repeatedly over a sequence of smaller potentials. The linear Sloan-Lawrence structure, based on Wideroe's work, used alternating charged drift tubes increasing in length to accommodate for the particles' increasing speed. The driving oscillator technology of the era limited the initial application of accelerators to heavy ions at low frequencies (order of MHz) and were ineffective at accelerating smaller particles like electrons [2]. At Stanford, Hansen's resonant radio-frequency (rf) cavities made possible higher frequencies and lower losses. This paved the way for the Varian brothers' klystron and higher available rf power [3]. And so continued the usual pattern of science: a limitation is reached and then removed by new technology. Synchrotrons, super-conducting accelerators, and free electron lasers are all accelerators structures developed to address different limitations on accelerator performance.

For what end? Large scale particle accelerators have been instrumental in our current understanding of how the universe behaves at the most fundamental level. The definition of what is the most basic building block of our world has rapidly evolved, or devolved as it were, from the chemical elements of the periodic table to individual atoms, to the more elusive elementary particles. Now immortalized in the form of a poster plastered to every physics classroom wall, the standard model began as a much smaller collection of

theorized particles that were confirmed and expanded upon as a direct result of high energy particle accelerator experiments.

Quarks, for instance, began as a hypothesis in 1964 to explain the composition of the numerous hadrons that had been discovered in the previous decade. Gell-Mann and Zweig both predicted three flavors of quarks and their anti-particles: up, down, and strange [4]. Initially viewed as a mathematical convenience, quarks' existence as elementary particles received further support in 1974. Experiments at both Stanford Linear Accelerator Center's two mile accelerator and Brookhaven National Laboratory's Alternating Gradient Synchrotron confirmed the existence of a fourth type: the charm quark [5] [6]. This made a lot of scientists happy for a very short period of time. The four quark flavors with fractional electric charges fit nicely together, but the symmetry was short lived. SLAC's immediate subsequent discovery of the tau lepton left a hole in the standard model; a hole suspiciously shaped like two new quarks [4]. A race for discovery commenced. The bottom quark was quickly confirmed at Fermilab's fixed-target experiment. The top quark followed two decades later, discovered at the Tevatron synchrotron accelerator, also at Fermilab [7].

It is acknowledged that a wider audience may be less enthralled at the prospect of experimentally confirming mathematical models of particles. The costly experiments are almost exclusively paid for by government funding, and fortunately the benefits to the individual tax payer are widespread and even tangible. Research for the sake of research drives the innovation of technology that has applications far beyond just the laboratory. For instance; one need only to glance at one's phone to reap the benefits of high-energy physics research. The World Wide Web was developed at CERN as an efficient way to

share and access high energy physics data through the internet in the early 1990's [8]. Additionally, particle accelerators directly impact daily life more than one might realize. X-rays and electron beams are an FDA-approved method to sterilize and preserve many types of food, such as fresh fruits and vegetables [9]. Most major hospitals will have at least one radiation therapy machine or isotope production cyclotron on-site. The semiconductor industry utilizes accelerators for ion implantation, making cheaper, more compact electronics possible [10].

With the benefits of particle accelerator research clear, present research aims to revolutionize entire accelerator systems, as well as to improve the designs of smaller individual components. At the beginning of every particle accelerator, there is a particle source. For electron accelerators, the particle source is typically an electron gun. Usually consisting of one to three rf cavities, the design of an electron gun depends on many factors, including its desired final particle energy. Accelerator centerline cavities are typically longitudinally symmetric, but for an initial cavity of an electron gun, a longitudinally asymmetric geometry is chosen to include an electron emitting cathode. Once a cavity geometry is set, one can explore the various methods of electron emission that the system might employ.

1.1. RF cavity design

An rf cavity is an enclosed conductive structure designed to increase a particle's energy by efficiently accommodating a specific electromagnetic mode. The simplest geometry is a metallic pillbox with no beam iris. The usual (and extremely effective) analogy is to compare the mechanics of this cylindrical metallic cavity to a resistor-inductor-capacitor (RLC) circuit.

1.1.1. Pillbox

Let's assume a single pillbox rf cavity with an oscillating electric field along the z-axis. This electric field *could* propagate a number of different ways, but here let's only consider the TM_{010} mode with the electric field lines running longitudinally down the z-axis. In the case of the first mode, it is easy to see the pillbox's end plates behave like a circuit's capacitor being driven at the frequency of the rf power source.

For a given voltage across parallel capacitor plates, the electric field between the plates scales inversely with the area of the plates. This fact holds true for rf cavities as well and can be used as a tool to focus the electric field, as will be seen later. This voltage differentiation between the two end plates must of course be accompanied by a current induced through the cavity's conducting walls. The cavity walls themselves are analogous to a resistor with an impedance value dependent on the material's surface resistance. As the electric field is oscillating, so too is the magnetic field curling around the inside of the cavity. A simple *N* turn inductor has a resulting voltage across the inductor proportional to the change in current in the loop, or change in flux through the loop. As will be seen with rf cavities, the inductance can be increased by increasing the

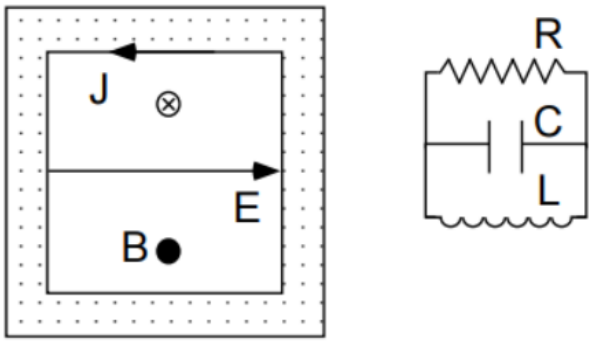

Figure 1-1: The rf cavity can be thought of as a lumped circuit, with its own resistance, capacitance, and inductance [11]

area over which the magnetic field is distributed. Generated and driven by the induced surface currents, the magnetic field oscillates π/2 out of phase with the electric field, as is the case with the circuit's inductor and its capacitor respectively.

$$C = \frac{Q}{V_C} = \frac{\epsilon_0 A}{d} \tag{1-1}$$

$$L = -V_L \left(\frac{dI}{dt}\right)^{-1} = -\frac{d\Phi_B}{dt}\left(\frac{dI}{dt}\right)^{-1} = \frac{\mu_0 N^2 A}{l} \tag{1-2}$$

$$\omega_0 = \sqrt{\frac{1}{LC} - \frac{R^2}{L^2}} \approx \sqrt{\frac{1}{LC}} \tag{1-3}$$

In both the circuit and cavity examples, the inductance can be thought of as containing energy stored within the structure at a particular phase in the cycle, while the resistance leads to energy loss in the structure. This π/2 phase difference occurs when the structures are operating at their resonant frequencies for a specific mode.

1.1.1.1. Resonant Frequency

To determine the resonant frequency of the pillbox, as previously mentioned, the focus will be the TM_{010} mode. The electric field has only a longitudinal component, and the magnetic field will only be in the azimuthal direction. Maxwell's equations for a cylinder then reduce to:

$$\frac{\partial^2 E_z}{\partial r^2} + \frac{1}{r}\frac{\partial E_z}{\partial r} = \frac{1}{c^2}\frac{\partial^2 E_z}{\partial t^2} \tag{1-4}$$

With the solution being of the exponential form (1-5). Solving (1-5) gives Bessel's zeroth order equation (1.6). For a conductor, $E_z(r) = 0$ at $r = R$, resulting in (1-7) [12].

$$E_z(r,t) = E(r)e^{i\omega t} \tag{1-5}$$

$$E(r) = E_0 J_0\left(\frac{\omega}{r}c\right) \tag{1-6}$$

$$2\pi f = \frac{2.405c}{R} \tag{1-7}$$

The resonant frequency's independence of length may seem counterintuitive, but recall the mode chosen: $TM_{010.}$ As the electric field is only a function of *r*, it does not vary longitudinally.

That's not to say that cavity length is inconsequential to the accelerator performance. Depending on the particle's velocity, the length of the cavity determines the range of the rf phase that is experienced by the particle. When connecting several pillboxes in series, cavity length then dictates how those pillboxes couple to each other. In other words: cavity length determines operating mode. Consider a series of pillboxes coupled by irises on axis, like a disk-loaded waveguide.

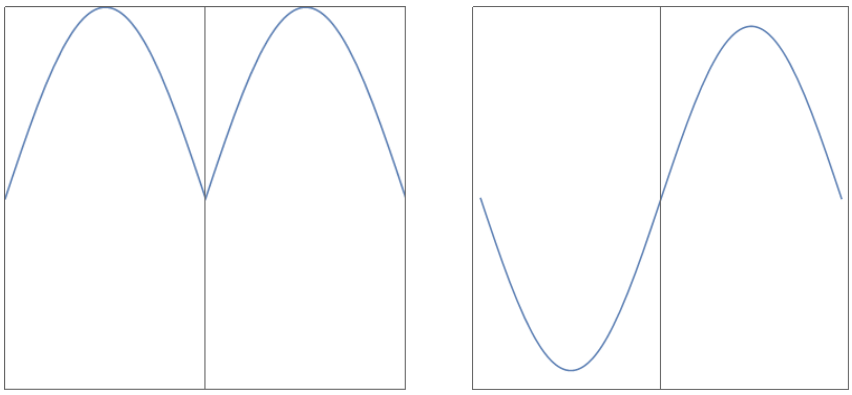

Figure 1-2: Example of a two pill box series at two different operating modes. Left: The two pillboxes have an rf phase identical to each other, known as the 0-mode. Right: The cavities rf phase are π out of phase with each other, known as the π-mode.

The rf power phase difference from one cavity to its neighbor is determined by its length. For example, if each cavity has a length equal to one half the rf wavelength, then each cavity would be 180 degrees (or π) off the phase from its neighbors. This is known as the π-mode. This operating mode is particularly useful for disk-loaded waveguides, as it allows a particle to gain energy in each cavity as it moves through, exiting the cavity just before the field oscillates to negative. The benefit of using a cavity with length $\lambda_{rf}/2$ becomes mathematically apparent when discussing another important cavity parameter: shunt impedance.

1.1.1.2. Shunt Impedance: Relativistic Case

With efficiency as a motivator, the design of a cavity should maximize the accelerating voltage achievable, given the power available. This parameter, known as shunt impedance, is defined as:

$$R_{shunt} = \frac{V_{acc}^2}{P_{diss}} \tag{1-8}$$

where, V_{acc} is the accelerating voltage (or energy gain per unit charge), and P_{diss} is the power dissipated into the cavity walls. It can be shown that shunt impedance is solely dependent on the particle's energy and injection phase as well as the cavity's geometry and material.

Take two infinite parallel plates in the x-y plane, each with a hole for a charged particle to pass through. Assume a sinusoidal voltage is applied at frequency ω_{rf} with phase φ, and the electric field between the two plates is uniform and a function of time, *t*.

$$E_z = E_z(t) = E_0 \, Cos(\omega_{rf} t + \varphi) \tag{1-9}$$

The energy gain per unit charge is:

$$V_{acc} = \int E_z(t)\, dt \tag{1-10}$$

By defining t=0 as the center between the two plates, (1-10) can be rewritten:

$$V_{acc} = E_0 Cos(\varphi) \int_{-t/2}^{t/2} Cos(\omega_{rf} t)\, dt \tag{1-11}$$

Integrating (1-11), where τ is the time it takes for the particle to traverse the cavity yields:

$$V_{acc} = \frac{2E_0}{\omega_{rf}} Cos(\varphi)\, Sin\left(\frac{\omega_{rf}\tau}{2}\right) \tag{1-12}$$

The particle's transit time can also be defined as the length of the cavity divided by the particle's velocity, c. [13] From here it is easy to identify why, for a particle with relativistic β= 1, it would be advantageous to set the length of the cavity to half of the rf wavelength. Referred to as the pi-mode, this geometry choice paired with injecting particles in-phase with the rf power would maximize the accelerating voltage (and thus the shunt impedance). In-phase implies that the particle is only in the cavity when the electric field is positive. However, not all of the energy in the cavity is available to the particle, as some power P_{diss} is dissipated in the cavity walls.

A result of the magnetic field penetrating the cavity walls and inducing surface currents, the power dissipated into the cavity material is dependent upon the material used, the excitation frequency, and inner surface area of the cavity. Surface resistivity (R_s), depends on the cavity material's conductivity (σ) and skin depth (δ), with the skin depth of a material being specific to the materials and the frequency.

$$P_{diss} = \frac{1}{2} R_s \int_{wall} \overrightarrow{H^2}\ dS \tag{1-13}$$

$$R_s = \frac{1}{\sigma\ \delta} \tag{1-14}$$

$$\delta = \sqrt{\frac{2}{\mu\ \sigma\ |\omega|}} \tag{1-15}$$

Note that the power dissipated depends on the magnetic field at the inner surface of the cavity. As will be elaborated later, increasing the inner volume of the cavity can reduce the magnetic field penetrating the cavity walls and increase the inductance. Minimizing the power dissipated into the cavity walls can also be achieved by proper material choice. Zero surface resistance is ideal, but it is only attainable with specific materials, such as niobium, cooled to superconducting temperatures (around 2-4 K). OFE copper, with a conductivity of 58 MS/m, is the usual choice for normal-conducting accelerators [14].

1.1.1.3. Shunt Impedance: Non-relativistic Case

At relativistic speed β~1 an accelerated particle's speed approaches *c*. At non-relativistic speeds, a particle can gain (and unfortunately lose) both energy and velocity. The power dissipated into the cavity walls remains straight forward to calculate, but determining the accelerating voltage experienced by lower energy particles requires tracking the particle's velocity and therefore position in the cavity over many sequential steps. By calculating the particle's change in energy Δε over some small *dz*, one can determine the particle's change in velocity in terms of the relativistic gamma (γ).

$$\Delta\varepsilon = \ qE_0 Cos(\varphi) \int Cos(\omega_{rf} t)\ dt = qE_0 Cos(\varphi) \int Cos\left(\omega_{rf} \frac{z}{\beta_n}\right)\ dz \tag{1-16}$$

$$\varepsilon_{n+1} = \varepsilon_n + \Delta\varepsilon \tag{1-17}$$

$$\beta_{n+1} = \sqrt{(\frac{\varepsilon_{n+1}}{\varepsilon_{rm}})^2 - 1} = \sqrt{\gamma_{n+1}^2 - 1} \tag{1-18}$$

Iterating over small enough increments of *dz* over the full length of the cavity produces the accelerating voltage experienced by the particle. To maximize shunt impedance at non-relativistic speeds, the cavity should be designed with the average kinetic energy of the particle in mind.

It is important to consider non-relativistic energies in cavity design for two main reasons. Electrons are not emitted at the speed of light, and therefore it is necessary to design structures to accelerate particles from lower energies to relativistic energies. Additionally, input power or efficiency requirements in some instances can only be met with lower field gradient structures.

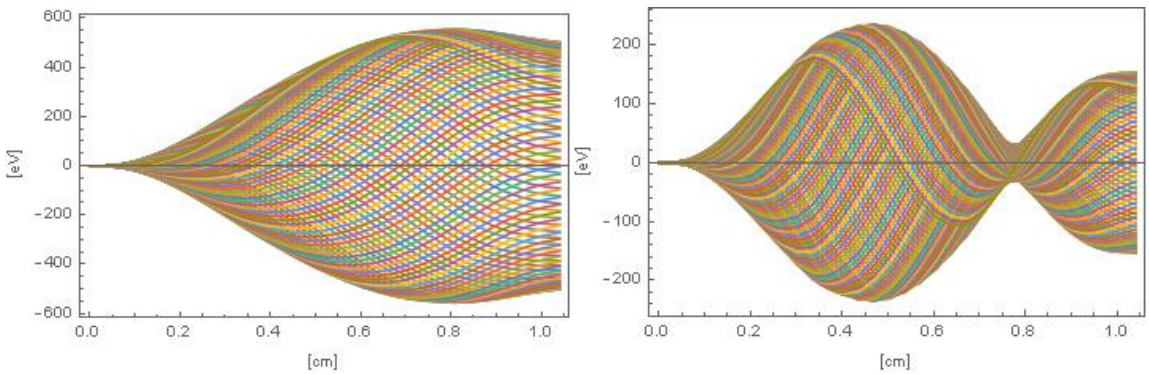

Figure 1-3: Particle's voltage as a function of position in the cavity over a sampling of all injection phases. Each colored trace denotes a different injection phase. Left: The particle has an average kinetic energy of 50 keV, and at certain injection phases, escapes the cavity shortly after the field flips to negative. Right: In the same cavity, a particle with 10 keV kinetic energy experiences more than one rf cycle. Even at optimal injection phase, a particle only gains ~120 eV. Electrons ending up with negative energy are moving backwards and typically lost.

1.1.1.4. Drawbacks of On-axis Coupling

Our original single pill box featured a longitudinal electric field with peak E_z on-axis. Adding an aperture to couple a series of pillboxes shifts the peak of E_z so that it is no longer on axis.

This decreases the voltage available to the particle and therefore the shunt impedance of the cavity. While the simple pillbox shape is useful as a starting point for a theoretical understanding of cavity design, in practice, the induced current in the cavity walls experiences significant resistance from the sharp corners of the cylinder. Because the rf power is coupling directly through the beam hole iris, the iris must be large. This reduces the on-axis electric field and therefore the accelerating voltage. On-axis coupling also presents manufacturing challenges. The resonant frequencies of the cavity are coupled to every other cavity in the accelerator, with immediate neighbors having the strongest

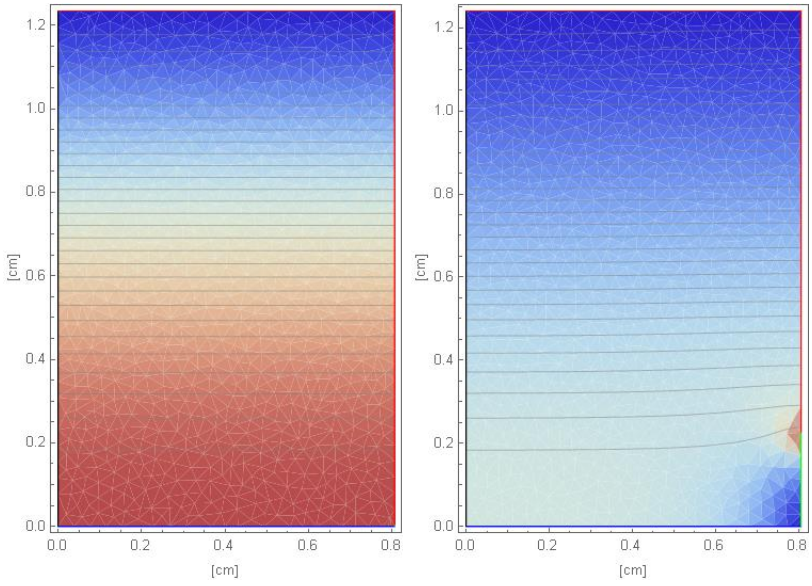

Figure 1-4: ¼ profile of the electric fields in a pillbox cavity. Left: Pillbox has no beam aperture and the peak electric field occurs down the accelerating centerline (x-axis). Right: The inclusion of a beam aperture shifts the electric field away from the path of the particle. Color scheme normalized to maximum field value (red).

coupling. Each cavity's resonant frequency, and therefore the resulting structure's resonant frequency, is extremely sensitive to machining errors. Once brazed together, measuring each cavity's resonant frequency is difficult, and methods for frequency adjustments (squeezing the radius of the cavity) are highly constrained.

1.1.1.5. Alternative Coupling Methods

There are two primary solutions to the constraints of on-axis coupling. The more common solution is to incorporate side-coupled cavities into the accelerator design. A side-cavity couples two centerline cavities by way of induction through rounded slits in both centerline cavities' bowls. The beam hole iris radius can therefore be much smaller than in the disk-loaded example, as the power coupling between cavities is no longer on-axis. The side cavities also decrease the waveguides sensitivity to tuning and machining errors. Because the number of cavities in the structure has effectively doubled, and all cavities couple to all other cavities, the resonant frequency of a single cavity is less affected by a single mistuned cavity. The centerline and side cavities of a side-coupled waveguide can both be tuned to higher frequencies. The side cavities, given their more exposed position, can also be tuned to a lower frequency by pressing on the ends of the cavity, effectively increasing their radius.

Side-coupling has been the standard in linear accelerator design for many decades. More recent accelerator designs have started to utilize distributed coupling. In this case, power is fed directly into each individual centerline cavity, rather than relying on large irises or side-cavities. This allows for smaller irises and higher on-axis fields. The coupling between cavities is therefore much smaller and in some cases can be neglected altogether.

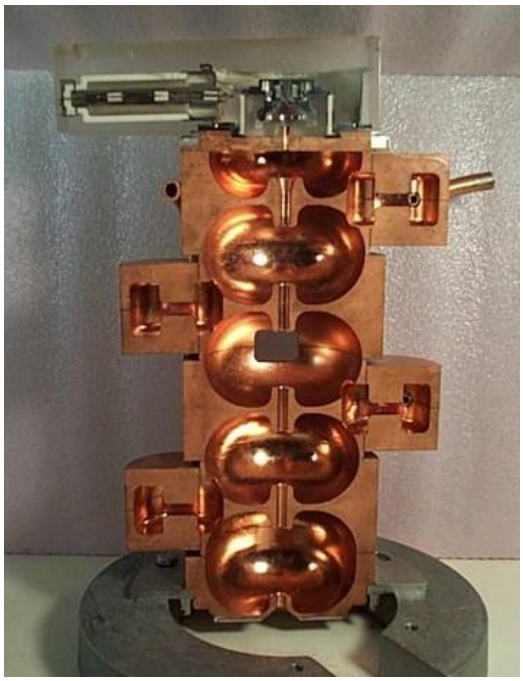

Figure 1-5: Cross-section of a side-coupled electron linear accelerator from Varian Medical Systems. With the side-cavities inductively coupled to the centerline, this guide operates at the π/2-mode [24].

Cavity geometry can then be fully optimized for high shunt impedance, without having to consider cell-to-cell coupling. The challenge with distributed coupling is to provide the correct phase of rf power to each cavity. Several successful solutions to this challenge exist [15].

1.1.2. Reentrant cavity

By modifying the cavity geometry, it is possible to decrease the magnetic field penetrating the inner cavity walls and increase the on-axis electric field, both of which increase shunt impedance. Reentrant cavities feature a curved inner bowl accompanied by rounded "noses" that protrude inward into the cavity space.

The bowl curvature accomplishes several things. Compared to the sharp corners of the pillbox, the curved reentrant cavity walls create less resistance for the induced current, meaning less power loss to the cavity walls. The bowl shape also increases the volume

Figure 1-6: Distributed coupling accelerator from Dymenso. A single brazing plane runs the entire length of the accelerator, and two tuning pins per cell (not shown) allow for frequency tuning.Photo courtesy of Dymenso LLC and Phillip Borchard.

occupied by the magnetic field and the inner surface in which the induced currents run [16].

The protruding nose serves to shape the electric field into the path of the particle, as the lack of conductive material in the beam-hole iris decreases the axial electric field. The specific curvature of the cavity noses (as well as the cavity bowl) decreases the capacitive area of the cavity and can be fine-tuned to maximize the shunt impedance of the cavity, given a length and desired resonant frequency.

1.2. Electron Emission

For an electron gun cathode, there are three possible electron emission methods. Thermionic emission ejects electrons from the cathode by increasing their kinetic energy. Field emission lowers the potential barrier of the cathode surface to allow for tunneling. Photo-electric emission utilizes the photo-electric effect.

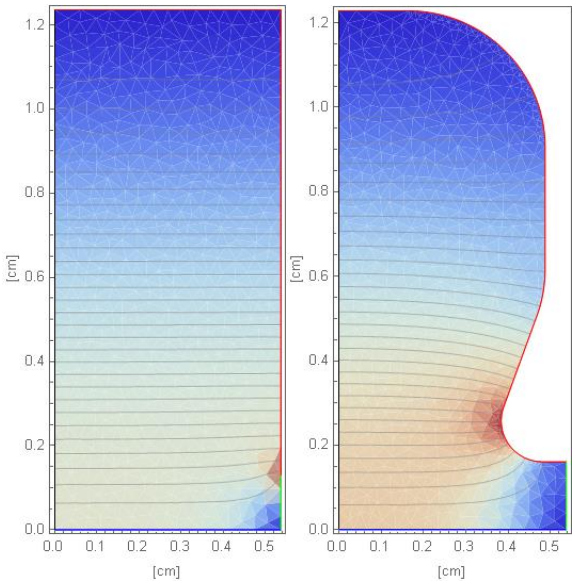

Figure 1-7: Two cavities with same basic dimensions, including beam aperture. The left reentrant cavity has a higher axial electric field along the accelerating centerline. Color scheme normalized to maximum field value (red).

1.2.1. Thermionic Emission

Heating metal increases the energy of the valence electrons within the metal. Electrons with sufficient energy may then escape the surface of the metal, and a positively charged anode can be placed some distance away from this metal cathode to draw away these escaped electrons. At lower voltages, the emission current is limited by space charge and the anode's ability to clear away electrons at the surface of the cathode. For a sufficient electric field between anode and cathode, the emission current can be considered independent of voltage and scales as a function of temperature only.

1.2.1.1. Child Langmuir Law

Using Helmholtz's decomposition, an electrostatic field can be described as the gradient of a scalar function. The electrostatic potential V (1-19). Using this description of the electric field, Gauss's Law becomes Poisson's Equation (1-20).

$$\vec{E} = -\vec{\nabla}V \tag{1-19}$$

$$\vec{\nabla}^2 V = \frac{\rho}{\epsilon} \tag{1-20}$$

By describing the volume charge density ρ in terms of current density (1-21) and using conservation of energy (1-22), (1-20) becomes (1-23):

$$\rho = \frac{\vec{J}}{\vec{v}} \tag{1-21}$$

$$\frac{1}{2}mv^2 = -qV \tag{1-22}$$

$$\vec{\nabla}^2 V = \frac{1}{\epsilon}\frac{J}{\sqrt{-2qmV}} \tag{1-23}$$

Imagine electrons with zero initial velocity being pulled off a cathode by a small potential gradient near its surface. The electron cloud forming at the surface of the cathode then lowers the potential to the point that electrons are then pushed onto the cathode – thus raising the potential and so-on. This balance forces the voltage at the surface of the cathode to be 0. Perpendicular to the surface of the cathode and at the surface of the cathode, the change in the potential is also 0. Given these boundary conditions, the second order differential equation can be solved to give an expression for the current density, also known as the Child-Langmuir Law [17]:

$$J = \left(\frac{4}{9}\epsilon\sqrt{\frac{2q}{m}}\frac{1}{x^2}\right)V^{3/2} \tag{1-24}$$

Where the leading term is called the perveance of the cathode and is solely a function of geometry. In this regime of thermionic emission, the current increases as the anode

voltage to the 3/2 power. However, at sufficiently high voltages, this emission curve is limited by the work function and temperature of the cathode material [18].

1.2.1.2. Richardson-Dushman Equation

For a metal plate cathode in the x-y plane, with electron charge *q*, the current density across the cathode plane can be written as:

$$J_z = \int q\, n(E) v_z(E) dE \tag{1-25}$$

Where *n(E)* is the density of electrons, $v_z(E)$ is the speed of the electrons in the $\hat{z}$ direction, and the expression is integrated over all energies of electrons that escape the metal cathode's potential barrier. The density of electrons *n(E)* can be rewritten as a product of the density of states, *g(E)*, and the probability that that state will occur, *f(E)*. Electrons follow the Fermi-Dirac distribution. With Planck's constant *h* and Boltzmann's constant k_B, the density of electrons in the cathode becomes:

$$g(E) = \frac{8\sqrt{2}\,\pi}{h^3}\, m^{3/2}\sqrt{E} \tag{1-26}$$

$$f(E) = \frac{1}{1 + e^{\frac{E-E_F}{k_B T}}} \tag{1-27}$$

Where E_F is the Fermi Energy, and only electrons with $E >> E_F$, have sufficient energy to escape the cathode's potential barrier. In this limit the exponential term in (1-27) will be large enough for *f(E)* to turn into the Boltzmann distribution:

$$f(E) = e^{-(\frac{E-E_F}{k_B T})} \tag{1-28}$$

As electrons in the cathode that have not yet escaped have zero potential energy, *E* can be written in terms of velocity. Combining this substitution with (1-26) and (1-28) gives:

$$J_z = q\,\frac{2\,m^3}{h^3}\,e^{\frac{E_F}{k_B T}}\int_{v_{min}}^{\infty} 4\,\pi\,v^2\,v_z(E)\,e^{-\frac{m\,v^2}{2\,k_B T}}\,dv \tag{1-29}$$

Integrating over all values of v_x and v_y, and considering the minimum energy required to escape the metal occurs when the kinetic energy is equal to the potential energy:

$$J_z = q\,\frac{2\,m^3}{h^3}\,e^{\frac{E_F}{k_B T}}\left(\sqrt{\frac{2\pi\,k_B T}{m}}\right)^2\int_{\sqrt{\frac{2U}{m}}}^{\infty} v_z(E)\,e^{-\frac{m\,v_z^2}{2\,k_B T}}\,dv_z \tag{1-30}$$

Grouping the leading constants from (1-31) into A_0, or the Richardson-Dushman constant, and substituting the material's work function for the Fermi energy less the potential energy required to escape the cathode material, yields (1-32), the Richardson-Dushman equation [18] [17]. For thermionic emission, the current density emitted from a cathode can be described using the Richardson-Dushman equation, which accounts for the material's work function and temperature.

$$j_{thermionic} = \frac{4\pi q m^2}{h^3}T^2 e^{\frac{-\varphi_w}{k_b T}} \tag{1-31}$$

$$j_{thermionic} = A_0 T^2 e^{\frac{-\varphi_w}{k_b T}} \tag{1-32}$$

It can be seen from the Richardson-Dushman equation (1-32) that the current emitted from a specific cathode material increases quadratically with temperature and appears to

have no limit. The cathode material only retains its integrity up to a certain temperature, thus limiting the practically achievable current.

1.2.2. Field Emission

Instead of increasing the electron's energy within the metal, field emission decreases the cathode material's potential barrier to allow electron tunneling. Specific emitter tip geometries are used to increase the effective field at the emitter tips.

1.2.2.1. Fowler-Nordheim Equation

Field emission relies on the quantum mechanical effect of electron tunneling through a potential barrier. Once the electron has escaped, it must also have enough kinetic energy to overcome the electrostatic force of its image charge.

The general equation for current density *J* induced by an electron tunneling in the z-direction through a potential barrier is identical to the thermionic distribution (1-25), with the addition of the tunneling probability $T(E_z)$:

$$J = q \int_0^\infty v_z \, T(E_z) \, n(E) \, dE \tag{1-33}$$

Where v_z is the particles velocity in the z-direction, $n(E)$ is the density of electrons with energy E, and $T(E_z)$ is the tunneling probability of an electron tunneling through a barrier in the z-direction. $n(E)$ can be found by taking the density of states $g(E)$ and the probability that those states will occur $f(E)$, and considering the particles are only tunneling in the z-direction (1-34). Integrating over all v_x and v_y and rewriting in terms of E yields (1-35). Using the identity (1-36) and relabeling variables produces (1-37):

$$J_z = q \int_0^{\infty} v_z \, dv_z T(E_z) \, \frac{2m^3}{h^3} f(E) \, dv_x dv_y \tag{1-34}$$

$$J_z = \frac{q \, 4\pi m}{h^3} \int_0^{\infty} dE_z T(E_z) \int_0^{\infty} f(E) \, dE \tag{1-35}$$

$$\int \frac{1}{e^x + 1} dx = -ln[e^{-x} + 1] \tag{1-36}$$

$$J_z = \frac{q \, 4\pi m k_B T}{h^3} \int_0^{\infty} dE_z T(E_z) \, ln\left[exp\left[\frac{E - E_F}{k_B T}\right] + 1\right] \tag{1-37}$$

To account for the potential barrier, $T(E_z)$ can be found using the Wentzel-Kramers-Brillouin (WKB) approximation for quantum mechanical tunneling:

$$T(E_z) = exp\left[-2\sqrt{\frac{8\pi^2 m}{h^2}} \int_0^{Ttun} \sqrt{q \, \Phi(z) - E_z} dz\right] \tag{1-38}$$

Where $q \, \Phi(z) - E_z$ is the energy difference between the potential barrier at z and the energy of the particle in the z-direction. T_{tun} is the location along z in which tunneling occurs. By considering this tunneling probability occurs when $E_z \approx E_F$, using the Taylor expansion and the fact that the potential barrier is equivalent to the effective electric field necessary to tunnel at T_{tun}, algebra gives:

$$J_z = \frac{q^2}{8\pi h \Phi} F_z^2 exp\left[-\frac{4}{3}\sqrt{\frac{8\pi^2 m}{h^2}} \frac{(q\Phi)^{3/2}}{q F_z}\right] \tag{1-39}$$

$$J_z = A F_z^2 exp\left[\frac{-B}{F_z}\right] \tag{1-40}$$

Grouping the two terms dependent on the work function of the material produces the Fowler-Nordheim equation for field emission, where temperature is assumed to be low. The effective field F is often expressed as $\beta * E$, where E is the nominal electric field and β is an enhancement factor dependent on geometry [19] [20].

Constants A and B are functions of the emitter material's work function and are well understood. Lanthanum hexaboride (LaB_6,) and cerium hexaboride (CeB_6) have very low work functions (2.7 and 2.65 eV, respectively) [21]. The field enhancement factor β depends on many poorly-known variables associated with the surface conditions, like the specific emitter tip shape, surface smoothness and surface cleanliness and in practice is determined from data. An experimental emitter tip array may have a typical enhancement factor value of around 30 [22].

2. Methods

To design an optimized electron gun cathode cavity, a simulation code must consider the geometric optimization of two longitudinally asymmetric halves of one cavity. The effort conducted here takes an existing optimization code and modifies it to optimize asymmetric geometries at non-relativistic energies.

The original optimization code is a custom finite element electromagnetic solver previously developed in C++ to solve azimuthally symmetric 2D problems, using Mathematica for the user interface[1]. This tool has been expanded to optimize an azimuthally symmetric half cavity geometry for a given optimization function using splines [22] [23]. However, geometric constraints and the addition of an emitter in the cavity require more flexibility in the functional form and freedom for the cavity.

2.1. Current Code

The geometric boundaries of the cavity are set using standard cavity parameters, such as radius and length, as well as elliptical inputs for the shape of the curves of the cavity bowl and reentrant nose, see Figure 2-1**.** The elliptical inputs are constrained to be within the cavity radius and length, with total angle of curvature restricted to $\pi/2$. Linear segments connect the geometric gaps between curves, see Figure 2-1. Elliptical parameters for physical impossibilities such as overlapping curves are forced to smaller values. Any automatic correction of input parameters is noted in the simulation output. Following the definition of the ½ cavity profile, the boundary conditions are set. See the rightmost illustration in Figure 2-1. Note that the edge of the cavity along the y-axis is

[1] Many thanks to the code's originator: Sami Tantawi (SLAC)

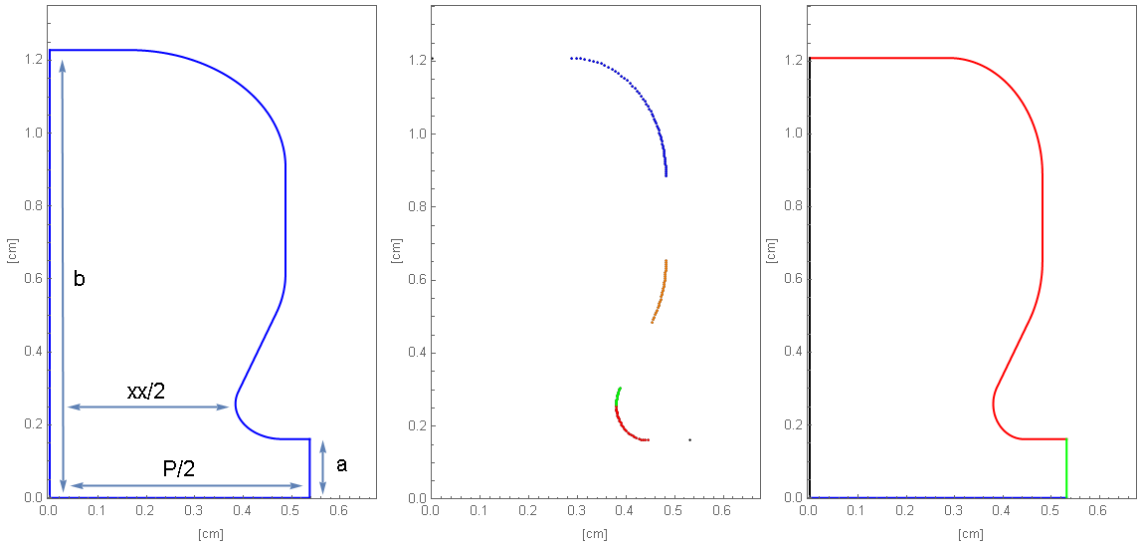

Figure 2-1 Left: Cavity parameters are fixed during optimization, with the exception of the nose depth xx. Center: Each ellipse is defined by its two axes; points are drawn over a maximum angle of π/2 to prevent sharp corners in the geometry. Tolerance for number of points is an adjustable input. Segments are colored to illustrate the four separate curves. Right: Boundary conditions for cavity geometry; red is resistive, green is perpendicular magnetic field, black is perpendicular electric field, and blue is the accelerating boundary.

defined to have a perpendicular electric field on the assumption of geometric (and therefore field) symmetry over the y-axis.

The resonant frequency of a cavity operating in the TM_{010} mode depends on its radius. The initial input of cavity radius, *b*, is tuned to correspond to the specified resonant frequency. The initial radius has a wide margin of acceptable error for which the code will correct, and any change in cavity radius is noted in the simulation output.

Using a triangular mesh, the electric and magnetic fields are calculated over the entire half cavity geometry. These fields provide values necessary to calculate cavity characteristics. The shunt impedance of the cavity is computed by calculating both the voltage gain of a particle passing through the cavity as well as the power dissipated into the cavity walls. To calculate voltage gain, the simulation generates the electric field

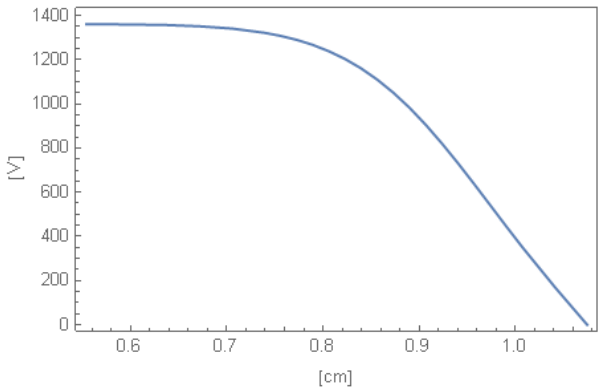

Figure 2-2: Axial electric field for half the cavity. This field is joined with its reflection across the y-axis for the axial field down the entire length of the cavity.

values along the accelerating boundary: the axial electric field. Because the simulation does this calculation on half of a symmetric cavity, the resulting field is then reflected across the y-axis to produce the axial electric field for the length of the entire cavity. The oscillating phase term of the rf input is included to calculate the net voltage gain experienced by the particle. The phase term assumes the particle is traveling at relativistic speeds and is being injected on-phase for acceleration.

$$V_{acc} = \int E(x) e^{i\,2\pi\,x/\lambda}\,dx \qquad 2\text{-}1$$

"On-phase" implies that the particle is only in the cavity when the electric field is positive. Depending on the desired operating mode, cavity length is typically between $\lambda/2$ and $\lambda/3$ for a relativistic particle. Cavity surface resistance (dependent on specified resonant frequency) and magnetic field values at the cavity's inner surface determine the power dissipated in the cavity. The code also generates the electric and magnetic fields along the surface of the cavity's resistive boundary, noting the maximum value for each.

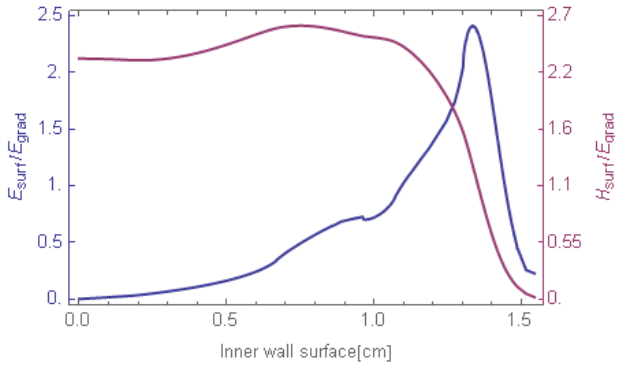

Figure 2-3: Electric and magnetic field values along the inner surface of the cavity, normalized to the electric gradient. The smooth transition in surface electric field values suggests smooth geometric transitions between ellipses.

With just the above functionalities, one could specify a cavity shape and hypothetically achieve an acceptable shunt impedance. This would involve making many minute adjustments to any or all geometric parameters, requiring prior experience in cavity design, time, effort, and patience. We propose instead to employ the simulation code to automatically maximize a certain optimization function, given flexible parameters such as the elliptical curves.

The optimization portion of the code incorporates a predefined function *G*. Using the Nelder-Mead method, the code maximizes *G* by adjusting (over a constrained range of values): the elliptical parameters, nose depth, and the angle at which the nose protrudes from the bowl of the cavity. The user defines parameter constraints and a starting interval for each of the variables. Reasonable values for the starting intervals depend primarily on cavity length and radius. With the goal of maximizing shunt impedance in mind, we chose the following expression for *G*:

$$G\left(R_{shunt}, E_{surfmax}, E_{grad}\right) = \frac{R_{shunt}}{\sqrt{1 + \left(\frac{E_{surfmax}/E_{grad}}{2.5}\right)^{20}}} \tag{2-2}$$

Where $E_{surfmax}$ is the maximum value of electric field over the entire inner surface of the cavity, and E_{grad} is the accelerating gradient over the length of the cavity. The function's denominator ensures that the shunt impedance is maximized without allowing excessively high surface fields. A higher ratio of surface electric field to gradient can be a sign of a sharp edge in the cavity creating a higher peak field, risking electric field break down. The limit of 2.5 was arrived at empirically. A high enough surface field in the cavity can become a source of electron field emission.

2.2. New Requirement: Non-relativistic Particle

By only considering a relativistic particle, the original simulation makes two assumptions: 1) the particle's velocity is equal to *c* and independent of its voltage gain within the cavity and, 2) the particle is injected on-phase. A particle is considered "non-relativistic" if its kinetic energy is at or below its rest mass (β <0.86). The only particles to be considered in this thesis will have velocities well below relativistic speeds, so velocity scales quadratically with particle kinetic energy, but we will consider a narrow-enough energy window to perform a linear approximation. We choose to define the

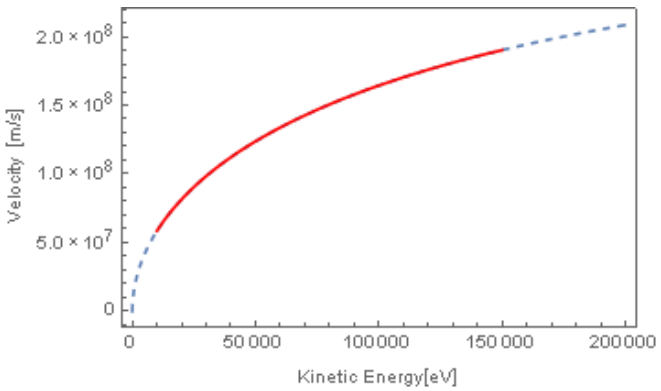

Figure 2-4: Electron's velocity as a function of kinetic energy. For the particle energy ranges discussed here, highlighted red region, and gradients of less than 100 keV/cm, the particles' velocities are approximated to scale linearly with energy.

average kinetic energy of the particle within the cavity to calculate an approximate energy gain.

The assumption of on-phase injection is no longer valid at non-relativistic speeds. Because it takes the particle longer than one half of an rf cycle to traverse the cavity, injecting on the incorrect phase could actually result in the particle being accelerated *backwards*. To determine the optimal phase to inject the non-relativistic particle, the particle is traced through the cavity over injection phases from $\theta = 0$ to π to determine maximum voltage gain.

$$V_{n+1} = Re\left[E(x)e^{i(\theta_n - \pi/2)}\right]dx + V_n \tag{2-3}$$

$$\theta_{n+1} = \theta_n + 2\pi f \frac{dx}{\beta c} \tag{2-4}$$

Injection phases of π to 2π which give negative acceleration are omitted. The shunt impedance of the cavity is then calculated using this maximum accelerating voltage. The rf power is assumed to be sinusoidal, with the axial electric field positive from 0 to π, and negative from π to 2π.

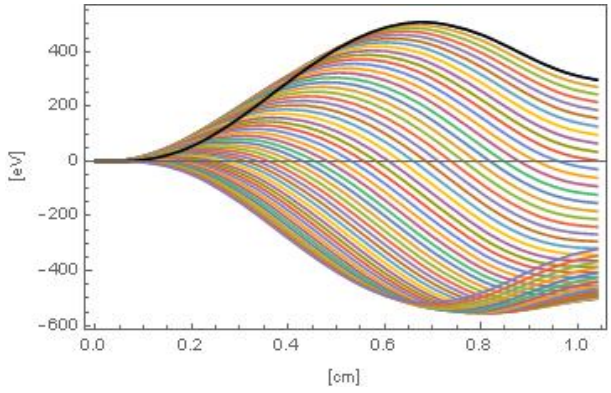

Figure 2-5: Particles injected at phases ranging from 0 to π. The injected particle with the highest exit energy that also never accelerated backwards is considered to have been injected at the optimum phase, see bold particle trace.

Non-relativistic edits to the optimization code were checked against the original code using the relativistic input of 100MeV average kinetic energy.

2.3. New Requirement: Asymmetric Cavity

To extend the simulation's application to electron gun cavity optimization, it is necessary to include asymmetric capabilities. Inputs should include different elliptical parameters for both halves of the cavity, as well as independent nose depths, iris radii, and half-cavity lengths. The only parameter constrained to be identical for both halves of the cavity is the bowl radius, *b,* to ensure smooth continuity between cavity halves. Azimuthal symmetry is still assumed. Boundary conditions are also modified, as there is no longer a perpendicular electric field boundary between the two halves. Both irises are set as perpendicular magnetic field boundaries. In the asymmetric case, the fields are calculated across the entire profile of the cavity.

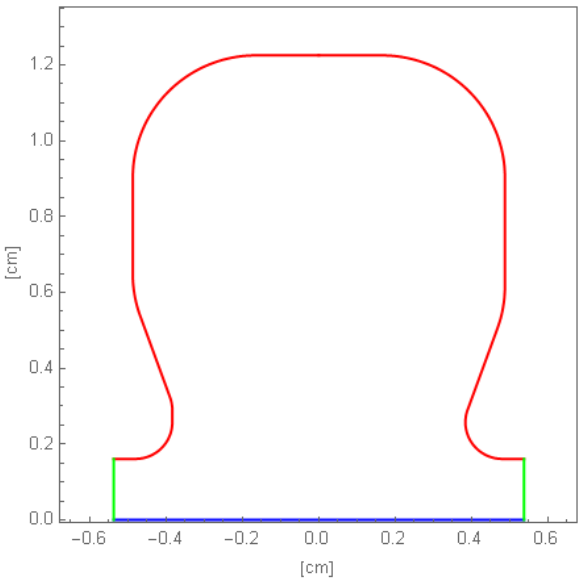

Figure 2-6 Boundary conditions for full cavity profile geometry; red is resistive, green is perpendicular magnetic field,, and blue is the accelerating boundary

The addition of asymmetrical capabilities complicates the optimization process. The code must consider twice as many variables to maximize *G*, with constraints and starting intervals of the parameters being unique to each half. Over-constrained inputs produce null results, while under-constrained inputs produce less than elegant cavity geometries. Often the result is an uninteresting "boxy" solution with all elliptical parameters equal to each other. Appropriate constraints and starting intervals for a set cavity radius scale loosely with cavity length.

2.4. Asymmetric Non-relativistic Inputs and Post-processing

The reason to accommodate asymmetric capabilities is to be able to model an electron gun emission cavity. One iris is set to a small value ~0.001 λ, as are the two elliptical parameters defining the nose curvature closest to the centerline. The resulting asymmetric axial electric field can be seen in Figure 2-7. It should be noted that the perpindicular magnetic field boundary on the left side is preserved. The code was not modified to accept an iris of radius of 0. Since the depth of the bowl curvature is

restricted to be within the length of the cavity, a reentrant design of this type includes a small vestige of unwanted cavity space included in the calculation.

For an iris equal to 0.001 λ, the electric field in this region of the cavity is on the order of 10^{-7} V/cm. An axial electric field is calculated for the entire length of the cavity, but a threshold is set to omit fields below ~10^{-5} V/cm, thus omitting this sliver. This region of the cavity is ignored for further calculations, but the calculation of power loss does include the appendage. As can be seen from Figure 2.7, the magnetic field in this region of the cavity is very small, as is the percentage of total surface area contained in this region, making this small systematic error negligible.

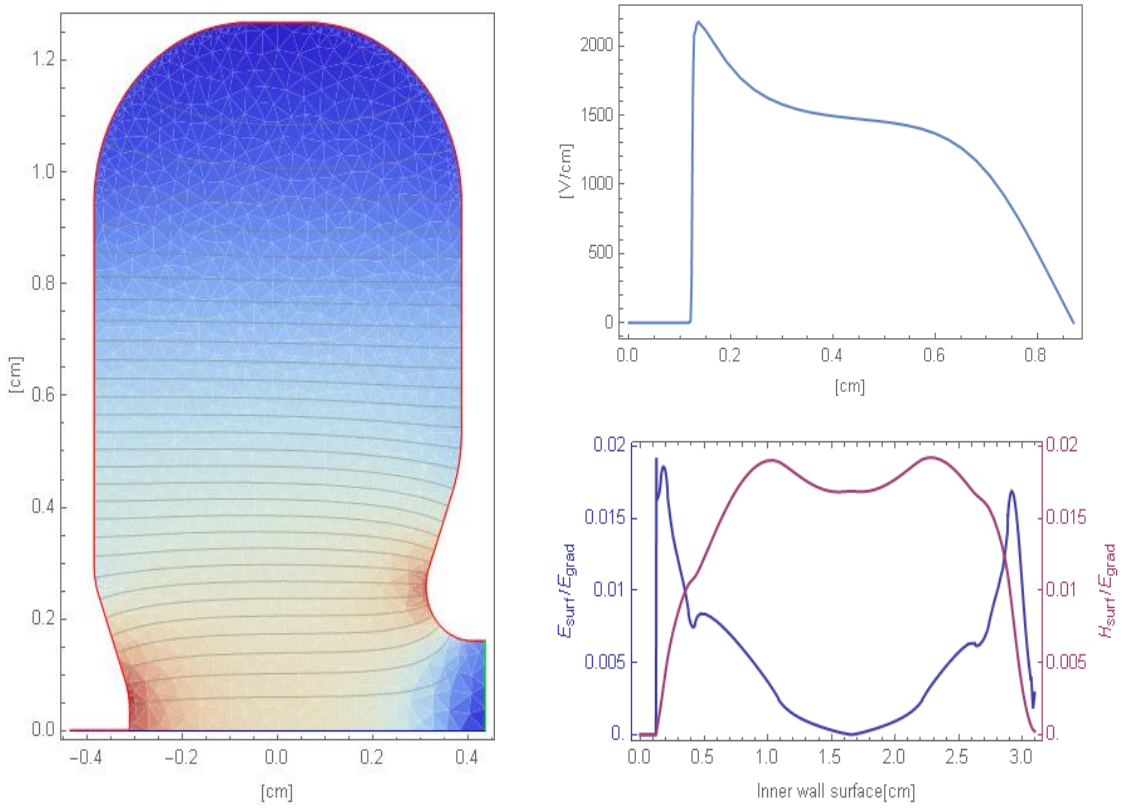

Figure 2-7: Left:Asymmetric cavity designed for a 100keV particle with cavity length ~0.2 λ. Color scheme normalized to maximum field value (red). Right, Top: Resulting axial electric field. Right, Bottom, surface fields normalized to gradient along the inner surface of the cavity.

A scaling factor is used to achieve a specified energy output. Cavities are designed for the average kinetic energy and total energy gain of the particle. The axial electric field is scaled accordingly, with cavity power loss scaling as the square of the scaling factor.

For cathode cavities, both thermionic and field emission are considered for a single geometric design. As discussed in section 2.2, the particle is traced over a range of injection energies. Output current density is generated by calculating the voltage at the cathode, which is the peak surface electric field, over the acceptable range of injection phases. The result is current density as a function of rf phase. For thermionic emission, the Child-Langmuir law will be used (2-5). For the peak current density achieved, the Richardson-Dushman equation will determine the minimum cathode temperature necessary to achieve that output (2-6). For field emission, the Fowler-Nordheim equation will be used (2-7).

$$J = \left(\frac{4}{9}\epsilon_0 \sqrt{\frac{2e}{m_e}}\frac{1}{\ell_{eff}^2}\right)V^{3/2} \tag{2-5}$$

$$j_{thermionic} = A_0 T^2 e^{\frac{-\Phi}{k_b T}} \tag{2-6}$$

$$J_z = A\ 10^{4.25\ \Phi^{-1/2}}\frac{\beta^2 E^2}{\Phi} exp\left[\frac{-B\Phi^{3/2}}{\beta\ E}\right] \tag{2-7}$$

Where ϵ_0 is the permittivity of free space, e is the charge of an electron, m_e is the mass of an electron, ℓ_{eff} is the effective cavity length (omitting the sliver of cavity mentioned above), A_0 is Richardson's constant 120 A/(cm^2 K^2) [17], A is (1.54 * 10^{-6} eVA/V^2), B is 6.83 * 10^9 V/(eV$^{3/2}$ m), β = 30, and the work function for LaB_6 (Φ = 2.7 eV) will be used [19].

This thesis designs and presents three initial electron gun cavities with asymmetrical cathode nose features with exit energies of 20, 40, and 100 keV. The peak surface electric field and acceptable injection phases of each cavity will then produce two current profiles; one via thermionic emission and one via field emission. The final design will be a series of three cavities: an initial 40keV emitter cavity with two subsequent reentrant cavities.

For the three cavity design, a single scaling factor is applied to all three cavities' electric field. The particle is traced through the series of cavities to identify the range of acceptable injection phases. For the three cavity system we treat the particle's changing velocity correctly without averaging. The total power loss of the series is summed over the length of the system for the total power dissipated. The power loss, the optimal injection phase, and total acceleration of the particle define the system shunt impedance.

3. Results

All cavities discussed will be X-band OFE copper cavities, designed to operate at 9.3 GHz, with 0.1 cm thick walls.

3.1. Single Emitter Cavity, 100 keV exit energy

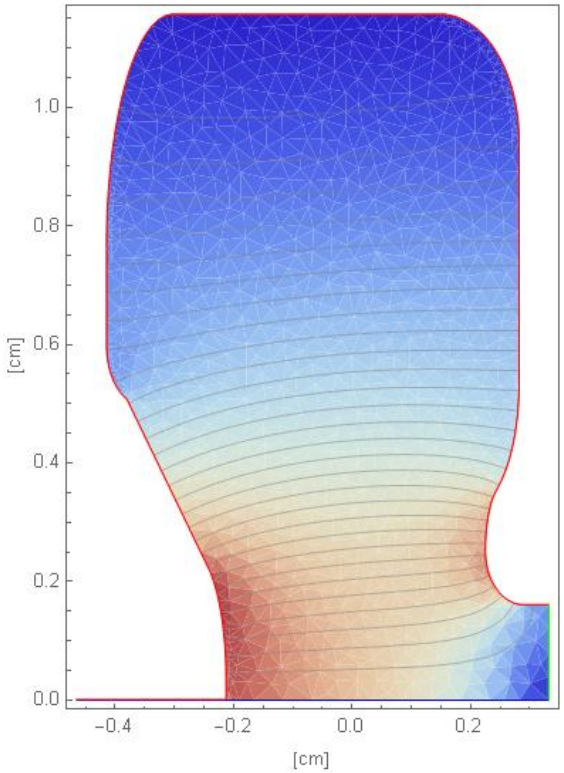

ℓ_{eff}	0.53 cm, 0.166λ
V_{acc}	100 keV
T_{avg}	50 keV
R_{shunt}	147 MΩ/m
$E_{surf\ max}$	40 MV/m
E_{grad}	18 MV/m
$E_{surf\ max}$ / E_{grad}	2.17
φ_{inj}	32.4 degrees
J_{peak}	0.08 A/cm^2
J_{peak} *thermionic*	
J_{peak} *field emission*	1.54 A/cm^2

Figure 3-1: Asymmetric emitter cavity designed for an exit energy of 100keV and performance values of interest. The left side of the cavity exhibits a slight oddity in the curvature from bowl to nose. Color scheme normalized to maximum field value (red).

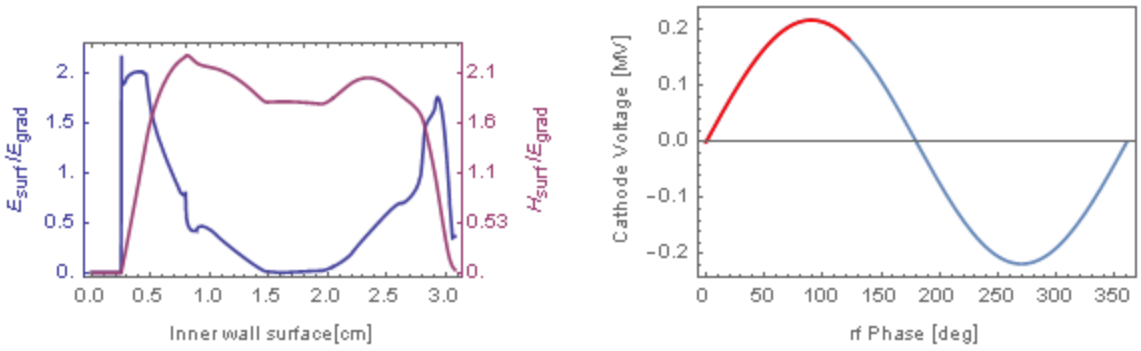

Figure 3-2 Left: Normalized with reference to the accelerating gradient, the surface electric and magnetic fields along the inner surface of the cavity. Right: rf electric field peak value over one oscillation, with acceptable injection phase range highlighted in red.

See Figure 3-1 for cavity profile shape and figures of merit. This cavity is designed to emit particles from the left side inner-wall and accelerate them to exit the right side at 100 keV. Figure 3-2 shows the electric and magnetic fields along the cavity's inner surface as a fraction of the accelerating gradient. The acceptable range of injection phases is shown in the left portion of Figure 3-2. The final set of plots in Figure 3-3 shows the emitted current as a function of injection phase.

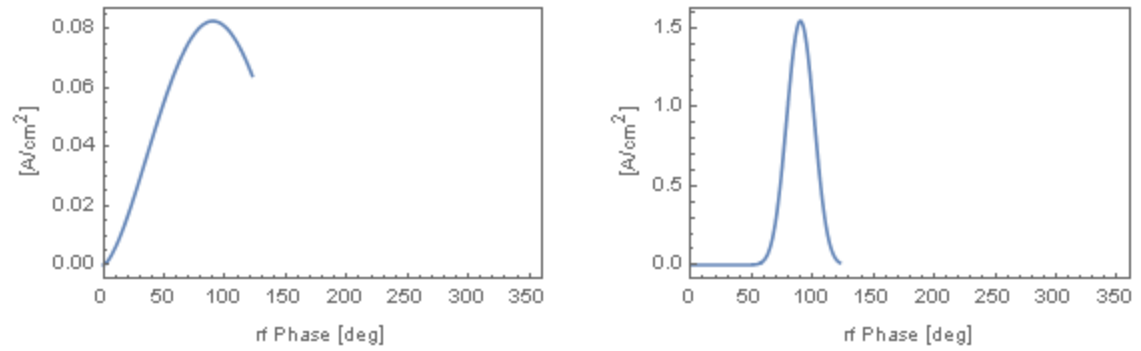

Figure 3-3: Left, current density emission curve for thermionic emission. Peak current of 0.08 A/cm^2 would require a LaB_6 cathode temperature of 1435K. Right, current density emission curve for field emission of a LaB_6 tip , with a peak current of 1.54 A/cm^2

3.2. Single Emitter Cavity, 40 keV exit energy

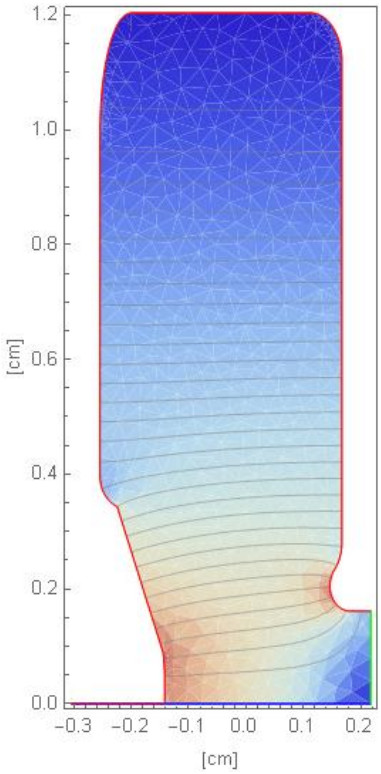

ℓ_{eff}	0.34 cm, 0.105λ
V_{acc}	40 keV
T_{avg}	20 keV
R_{shunt}	90 MΩ/m
$E_{surf\ max}$	29 MV/m
E_{grad}	11 MV/m
$E_{surf\ max}$ / E_{grad}	2.49
φ_{inj}	36 degrees
J_{peak} *thermionic*	0.06 A/cm^2
J_{peak} *field emission*	0.07 mA/cm^2

Figure 3-4: Asymmetric emitter cavity designed for an exit energy of 40keV and performance values of interest. Color scheme normalized to maximum field value (red). The left side of the cavity again exhibits a slight oddity in the curvature from bowl to nose.

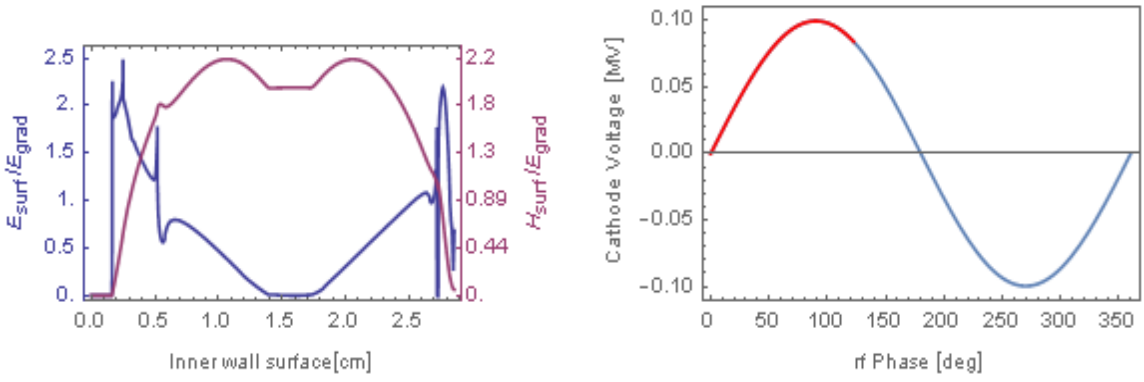

Figure 3-5: Left: Normalized with reference to the accelerating gradient, the surface electric and magnetic fields along the inner surface of the cavity. The electric field exhibits more sharp peaks as compared to the 100 keV cavity. Right: rf electric field peak value over one oscillation, with acceptable injection phase range highlighted in red.

See Figure 3-4 for cavity profile shape and figures of merit. This cavity is designed to emit particles from the left side and accelerate them to exit the right side at 40 keV. As in the 100keV case, the region of the cathode side where the bowl transitions to the nose has an undesirable corner-like geometry. Figure 3-5 shows the electric and magnetic fields along the cavity's inner surface relative to the accelerating gradient. Here the electric field values have much sharper peaks, note the peak around 0.5 cm where the bowl to nose transition forms a pseudo-corner. The acceptable range of injection phases is noted in the left part of Figure 3-5. The final set of plots in Figure 3-6 shows the emitted current as a function of injection phase. The peak surface electric field in this cavity is approximately half that of the 100keV cavity, but the resulting field emission current is over four orders of magnitude smaller.

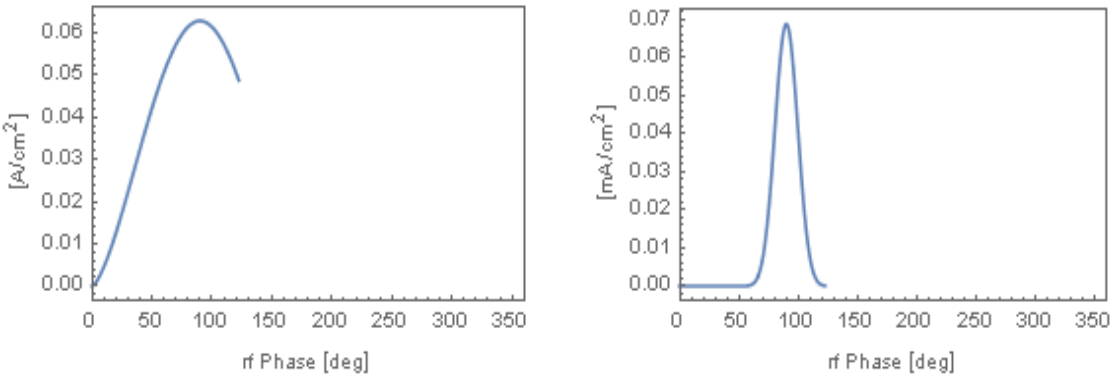

Figure 3-6 Left, current density emission curve for thermionic emission. Peak current of 0.06 A/cm^2 would require a LaB_6 cathode temperature of 1419K. Right, current density emission curve for field emission of a LaB_6 tip, with a peak current of 0.07 mA/cm^2

3.3. Single Emitter Cavity, 20 keV exit energy

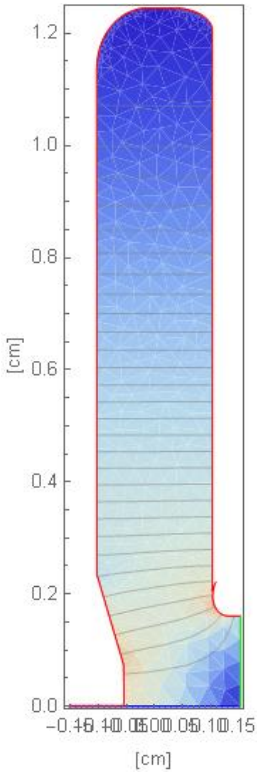

ℓ_{eff}	0.21 cm, 0.065λ
V_{acc}	20 keV
T_{avg}	10 keV
R_{shunt}	32 MΩ/m
$E_{surf\ max}$	31 MV/m
E_{grad}	9.6 MV/m
$E_{surf\ max} / E_{grad}$	3.29
φ_{inj}	43 degrees
J_{peak} *thermionic*	0.09 A/cm^2
J_{peak} *field emission*	1.02 mA/cm^2

Figure 3-7 Asymmetric emitter cavity designed for an exit energy of 20keV and performance values of interest. Color scheme normalized to maximum field value (red). The right side of the cavity has a small but sharp switchback that is creating a peak surface electric field on the non-cathode side of the cavity.

The optimized 20keV cathode cavity included a different geometric anomaly. The transition from bowl to nose on the right side of the cavity contains a sharp point in the geometry, creating the peak surface electric field on the anode side of the cavity, see Figure 3-8. This surface electric field has little contribution to the acceleration of the particle, given its location. Thus the field at this point has to be very high for the on-axis field to be high enough to achieve the accelerating voltage desired. If the cathode were intended to be on the right side, it would have a decent current output, see Figure 3-9.

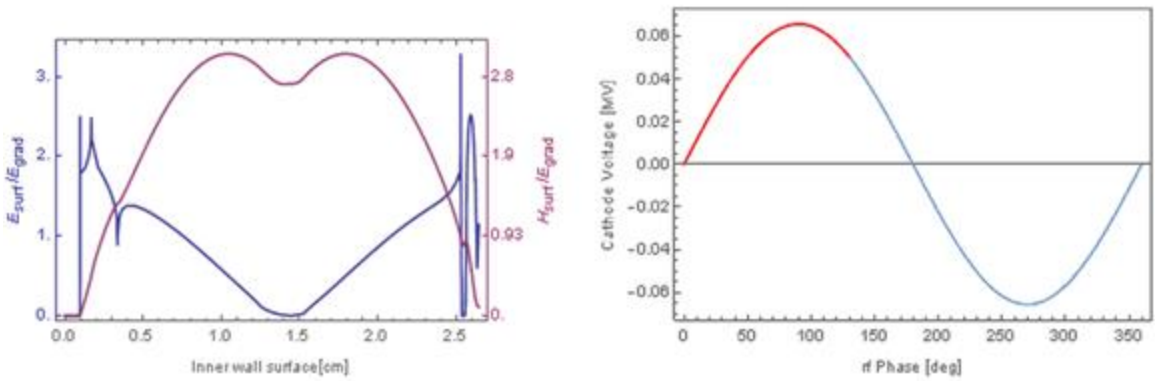

Figure 3-8: Left, the peak surface electric field is on the right side and has a much higher ratio to gradient than in the previous two cases. Right: rf electric field peak value over one oscillation, with acceptable injection phase range highlighted in red.

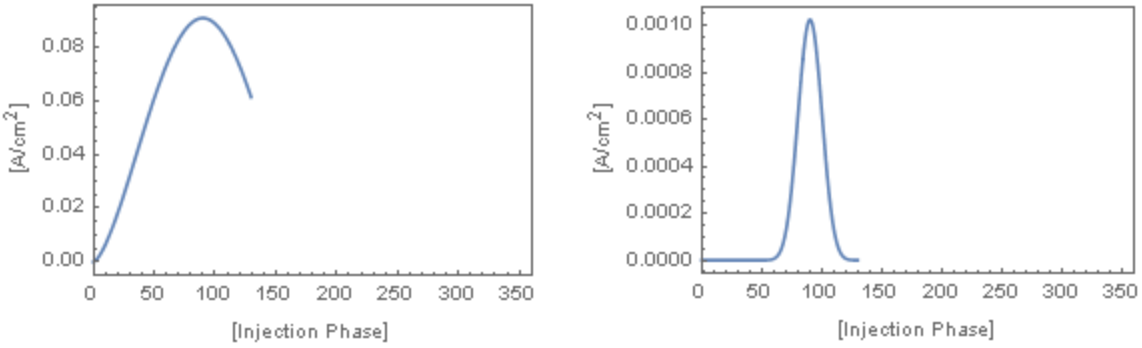

Figure 3-9: Left, thermionic, and right, field emission curves for 20keV cavity. The voltage inputs were based on the peak surface electric field, which in this case in on the non-cathode side of the cavity.

3.4. Series of 3 cavities

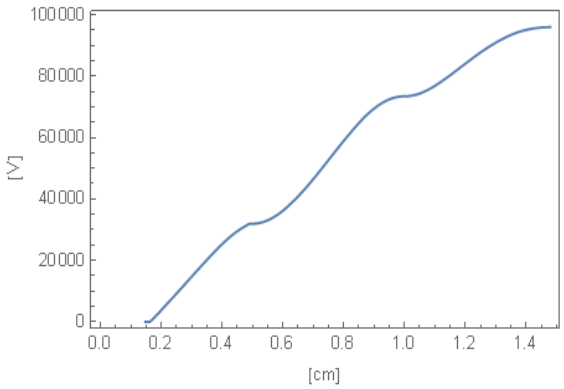

$\ell_{eff,\ total}$	1.35 cm
$\ell_{eff,\ 1}$	0.342 cm
$\ell_{eff,\ 2}$	0.503 cm
$\ell_{eff,\ 3}$	0.503 cm
$V_{acc,\ total}$	95 keV
$V_{acc,\ 1}$	31 keV
$V_{acc,\ 2}$	42 keV
$V_{acc,\ 3}$	22 keV
$R_{shunt,\ total}$	44.3 MΩ/m
$E_{grad,\ total}$	7.12 MV/m
$E_{surf\ max\ 1}$	29 MV/m
J_{peak} *thermionic*	0.06 A/cm^2
J_{peak} *field emission*	0.05 mA/cm^2

Figure 3-10: Left: Particle injected at optimum phase for energy gain. The transition between cavities can be seen around 0.4 and 1.1 cm. Right: Effective length and acceleration of the entire system and per individual cavity.

Three cavities were optimized separately, then the particle was traced through all three axial electric fields, operating in the π-mode, to find an optimal injection phase. The initial cathode cavity is the same design from section 3.2; the 40 keV exit energy cathode cavity. The second and third were symmetric cavities of the same design.

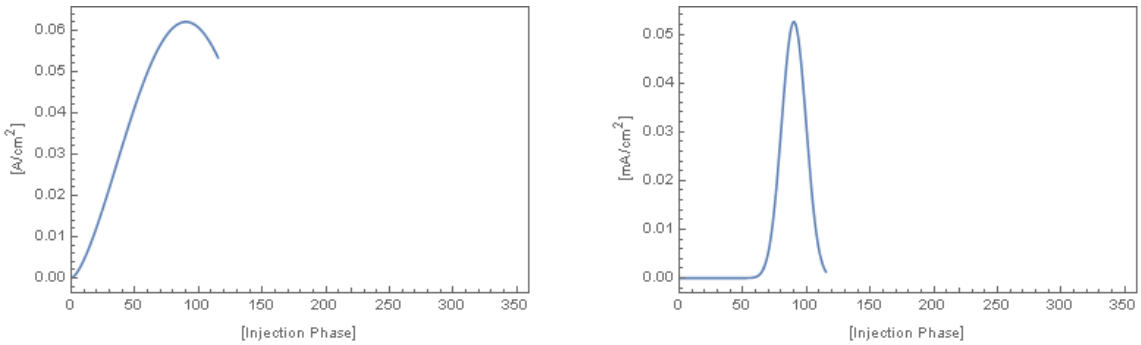

Figure 3-11: Utilizing the peak surface field of the cathode cavity, and the acceptable injection phases of the system, thermionic emission (left) achieves a peak current density of 0.06 A/cm^2. A peak current density of this value would require a cathode temperature of 1400 K. Field emission (right) achieves a peak current density of 0.05 mA/cm^2.

4. Discussion

The most successful of all the designs reported is the 100 keV cavity, and this can be attributed to the successful optimization of its geometry. The 20 keV cavity contained a sharp point, and the 40 keV cavity had a more exaggerated "corner" geometry as compared to the 100 keV cavity. The higher energy cavity also exhibited a much smoother distribution of the electric field along its inner surface. For the discussed thermionic output of all cavity designs, temperature would not have been a limiting factor for the cathode. All peak current densities fell below normal cathode operating temperatures, around 1600-2000 K.

The three cavity stack proved very capable of meeting low current needs. Higher currents would require further design modification, such as using a cathode metal with a lower work function or implementing a field emission tip with a higher field enhancement factor.

It is worth noting that the power requirements for the individual cavity designs discussed are quite low. The 100 keV cavity requires 68 W average power, while the 40 keV and 20 keV cavities only require only 17 W and 12 W respectively.

There are clear areas of improvement that could make this optimization program facilitate gun design more easily. Stacking the three cavities into a single unit proved to be a laborious task, as each optimization was done in series, with only user input to communicate one cavity's output to another. A single Mathematica program could be devised to design three cavities together, such that the output of the first design feeds into

the next. This single program should utilize a single scaling factor over all three cavities' fields.

The optimizer requires very specific ranges of acceptable elliptical parameters, especially with the shorter cavities. Even over one hundred iterations, often the most optimal cavity still contained jagged edges between the nose's elliptical curves. Not only are these sorts of shapes non-machinable, they are also generally undesirable shapes. For instances other than an intentional array of electron emitter tips, a sharp edge point and the extremely high surface electric field it brings with it can cause unintentionally emitted electrons and field breakdown. This geometric issue would not affect lower frequency designs. The optimization code would be very successful at designing, for instance, low gradient S-band cavities.

Because the lengths of the two cavity halves are not optimized, the output parameters of the cavity are limited by the selection of the cavity length and cavity length to nose depth ratio which is iterated upon. Generally, the optimal cavity length is between $\lambda/2$ and $\lambda/3$. The creation of the "null" sliver of space on the left-hand side complicates that decision, as does the ability to skew which side of the cavity contains more or less of the entire cavity length. Including the cavity length as an optimized parameter would not be possible with the code in its current form. Because the cavity length, in part, bounds the limits of the elliptical curves, adding cavity length as another variable would result in an inefficient optimizer. It might be worth exploring holding some elliptical parameters constant while varying cavity length and nose depth. This feature would be especially useful for stacking a multiple-cavity system.

Further development of this optimization code should include the capability to eliminate the iris on one (or both) sides of the cavity design. Part of the input parameters could be removing the perfect magnetic conductor boundary and having the resistive boundary meet the accelerating boundary. For the shorter cavities at lower energies, a new list of optimizing constraints and starting intervals should be explored. The shorter cavities were prone to overlapping elliptical curves and sharp edges. Future modifications of the code should investigate how best to modify the maximizing function constraints to both increase shunt impedance while also not creating sharp tips and therefore excessively high peak surface electric fields.

References

[1] H. L. e. a. Matis, "Particle Accelerators," in *Nuclear Science—A Guide to the Nuclear Science Wall Chart*, 4th ed., Lawrence Berkeley National Laboratory, Contemporary Physics Education Project (CPEP), 2018.

[2] B. J. Holzer, "Introduction to Particle Accelerators and their Limitations," *CAS-CERN Accelerator School: Plasma Wake Acceleration,* pp. 30-33, 2014.

[3] G. Caryotakis, "High Power Klystrons: Theory and Practice at the Stanford Linear Accelerator Center," *SLAC-PUB-10620,* pp. 5-10, 2005.

[4] B. Carithers and P. Grannis, "Discovery of the Top Quark," *Beam Line,* vol. 25, no. 3, pp. 4-9, Stanford Linear Accelerator Center.

[5] "November 1974: Discovery of the Charmed Quark," *American Physical Society,* vol. 26, no. 10, pp. 2-3, 2017.

[6] "Brookhaven and the Nobel Prize," [Online]. Available: https://www.bnl.gov/bnlweb/history/nobel/1976.php. [Accessed January 2019].

[7] "Key Discoveries," Fermilab, 2016. [Online]. Available: http://www.fnal.gov/pub/science/particle-physics/key-discoveries.html. [Accessed August 2018].

[8] B. White, "The World Wide Web and High Energy Physics," *SLAC-PUB-7757,* 1998.

[9] "Food Irradiation: What You Need to Know," *FDA Resource Library,* June 2016.

[10] G. Roberts Jr., "Semiconductors: Accelerator-powered ion implantation proves key to advances in integrated circuits," *Symmetry Magazine,* 2014.

[11] D. Whittum, "Introduction to Microwave Linacs," *SLAC-PUB 8026,* p. 9, 1998.

[12] D. A. Edwards and M. J. Syphers, An Introduction to the Physics of High Energy Accelerators, Dallas: Wiley-VCH, 2004.

[13] S. Cousineau, J. Holmes and Y. Zhang, "Fundamentals of Accelerator Physics; Lecture 3: RF Acceleration in Linacs," Winter 2011. [Online]. Available: http://uspas.fnal.gov/materials/11ODU/Lecture3_Particle_Acceleration_2.pdf.

[14] U. S. D. o. Commerce, "Copper Wire Tables," vol. Circular of the Bureau of Standards, no. 31, 3rd ed, 1914.

[15] S. Tantawi, M. Nasr, L. Zenghai, C. Limborg and P. Borchard, "Distributed Coupling Accelerator Structures: A New Paradigm for High Gradient," *ArXiv,* vol. 1811.09925v1, November 2018.

[16] E. Jensen, "RF Cavity Design," *ArXiv,* vol. 1601.05230, 2007.

[17] M. Grilj, "Thermionic Emission," in *University of Ljubljana Department of Physics Seminar,* Ljubljana, 2008.

[18] A. S. Gilmour Jr., Klystrons, Traveling Wave Tubes, Magnetrons, Crossed-Field Amplifiers, and Gyrotrons, Norwood: Artech House, 2011.

[19] J. W. Wang and G. A. Loew, "Field Emission and RF Breakdown in High-Gradient Room-Temperature Linac Structures," *SLAC-PUB 7684*, 1997.

[20] D. Ng Keh Ting, "Synthesis and characterization of gallium nitride nanowires by pulsed laser ablation," *Scholar Bank National University of Singapore*, pp. 157-170, 2008.

[21] "Applied Physics Lanthanum and Cerium Hexaboride (LaB6 and CeB6) Filaments / Cathodes," Electron Microscopy Sciences, [Online]. Available: https://www.emsdiasum.com/microscopy/products/microscope/lab6_ceb6.aspx. [Accessed 2019].

[22] P. Piot, "First Operation of an Ungated Diamond Field-Emission Array Cathode in a L-Band Radiofrequency Electron Source," *arXiv:1402.6999*, 2014.

[23] A. Gold and S. Tantawi, "A 2D Steady-State Space Charge Solver for Azimuthally Symmetric Problems of Arbitrary Degree," in *9th Int. Particle Accelerator Conf.(IPAC'18)*, Vancouver, BC, Canada, JACOW Publishing, Geneva, Switzerland, April 29-May 4, 2018.

[24] M. Nasr and S. Tantawi, "New Geometrical-Optimization Approach Using Splines for Enhanced Accelerator Cavities' Performance," *IPAC*, Vols. 0.18429/JACoW-IPAC2018-THPMK049, 2018.

[25] M. Trail, "Microwave Electron Linear Accelerators for Cancer Therapy and Non-destructive Testing: History, Applications, and Theory," in *University of Idaho Research Colloquium* , 2008.